

# Multi-scale additive manufacturing of 3D porous networks integrated with hydrogel for sustained in vitro tissue growth

Li, J.; Isaakidou, A.; van Zanten, L. J.; Tas, R. P.; Mirzaali, M. J.; Fratila-Apachitei, L. E.; Zadpoor, A. A.

10.1016/j.actbio.2025.03.005

**Publication date** 

**Document Version** Final published version Published in Acta Biomaterialia

Citation (APA)

Li, J., Isaakidou, A., van Zanten, L. J., Tas, R. P., Mirzaali, M. J., Fratila-Apachitei, L. E., & Zadpoor, A. A. (2025). Multi-scale additive manufacturing of 3D porous networks integrated with hydrogel for sustained in vitro tissue growth. *Acta Biomaterialia*, *196*, 198-212. https://doi.org/10.1016/j.actbio.2025.03.005

Important note

To cite this publication, please use the final published version (if applicable). Please check the document version above.

Copyright

Other than for strictly personal use, it is not permitted to download, forward or distribute the text or part of it, without the consent of the author(s) and/or copyright holder(s), unless the work is under an open content license such as Creative Commons.

Please contact us and provide details if you believe this document breaches copyrights. We will remove access to the work immediately and investigate your claim.

ELSEVIER

Contents lists available at ScienceDirect

# Acta Biomaterialia

journal homepage: www.elsevier.com/locate/actbio



# Full length article



# Multi-scale additive manufacturing of 3D porous networks integrated with hydrogel for sustained *in vitro* tissue growth

J. Li \*0, A. Isaakidou 0, L.J. van Zanten, R.P. Tas, M.J. Mirzaali, L.E. Fratila-Apachitei \*, A.A. Zadpoor

Department of Biomechanical Engineering, Faculty of Mechanical Engineering, Delft University of Technology (TU Delft), Mekelweg 2, Delft 2628 CD, The Netherlands

#### ARTICLE INFO

# Keywords: Additive manufacturing 3D porous channel networks Diffusion Hydrogels in vitro tissue model

#### ABSTRACT

The development of high-fidelity three-dimensional (3D) tissue models can minimize the need for animal models in clinical medicine and drug development. However, physical limitations regarding the distances within which diffusion processes are effective impose limitations on the size of such constructs. That is because larger-size constructs experience necrosis, especially in their centers, due to the cells residing deep inside such constructs not receiving enough oxygen and nutrients. This hampers the sustained in vitro growth of the tissues which is required for achieving functional microtissues. To address this challenge, we used three types of 3D printing technologies to create perfusable networks at different length scales and integrate them into such constructs. Toward this aim, networks incorporating porous conduits with increasingly complex configurations were designed and fabricated using fused deposition modeling, stereolithography, and two-photon polymerization while optimizing the printing conditions for each of these technologies. Furthermore, following network embedding in hydrogels, contrast agent-enhanced micro-computed tomography and confocal fluorescence microscopy were employed to characterize one of the essential network functionalities, namely the diffusion function. The investigations revealed the effects of various design parameters on the diffusion behavior of the porous conduits over 24 h. We found that the number of pores exerts the most significant influence on the diffusion behavior of the contrast agent, followed by variations in the pore size and hydrogel concentration. The analytical approach and the findings of this study establish a solid base for a new technological platform to fabricate perfusable multiscale 3D porous networks with complex designs while enabling the customization of diffusion characteristics to meet specific requirements for sustained in vitro tissue growth.

Statement of significance: This study addresses an essential limitation of current 3D tissue engineering, namely, sustaining tissue viability in larger constructs through optimized nutrient and oxygen delivery. By utilizing advanced 3D printing techniques this research proposes the fabrication of perfusable, multiscale and customizable networks that enhance diffusion and enable cell access to essential nutrients throughout the construct. The findings highlighted the role of network characteristics on the diffusion of a model compound within a hydrogel matrix. This work represents a promising technological platform for creating advanced *in vitro* 3D tissue models that can reduce the use of animal models in research involving tissue regeneration, disease models and drug development.

#### 1. Introduction

As life expectancy continues to increase, continued improvement of medical treatments, curing of chronic diseases, and more efficient healthcare systems become increasingly challenging. For example, drug screening for providing cost-effective and targeted drugs and treatments [1] is limited by the need for animal models to assess the safety and

efficacy of the drug before clinical use. *In vitro* models can serve either as an important alternative to *in vivo* models or an additional tool for drug screening provided they are clinically relevant [2–5].

It is generally accepted that cell growth in 3D *in vitro* models may more accurately reflect the *in vivo* tissue microenvironment than 2D cell cultures [2]. Therefore, continuous efforts are focused on developing such models to study the etiology and progress of diseases, to test the

E-mail addresses: J.Li-23@tudelft.nl (J. Li), E.L.Fratila-Apachitei@tudelft.nl (L.E. Fratila-Apachitei).

https://doi.org/10.1016/j.actbio.2025.03.005

<sup>\*</sup> Corresponding authors.

toxicity and therapeutic effects of new drugs, to generate functional microtissues for tissue engineering or transplantation, and for regenerative approaches to restore the function of failed tissues. Examples include models for cancer [6-9], heart [10-13], liver [14-18], and lung [19,20] diseases, as well as vascularized tissue models [21-25].

While engineering *in vitro* models continues to make progress in reproducing the physiology and anatomy of human tissues and organs *in vitro* [26,27], several challenges are still encountered, such as model scalability for industrial and clinical applications, efficient *in vitro* tissue vascularization and perfusion, and the sustained *in vitro* growth of functional tissues [28–30].

One of the major causes of these challenges is represented by the limited diffusion of nutrients and oxygen throughout the 3D constructs which can lead to adverse effects on cell metabolism and function, and eventually lead to local tissue necrosis [31–33]. As a result, the size of such tissues can only reach several hundred microns to a few millimeters, depending on the tissue type [33]. At the same time, for most applications, it is necessary to simultaneously culture multiple cell types in different areas of the construct [34], guide cell differentiation by supplying specific factors, maintain long-term tissue growth and functionality through stable supply and exchange of nutrients, oxygen, bioactive agents, and metabolites [35–37].

From an engineering perspective, these challenges are addressed by various approaches. One of the most investigated approaches relies on the generation of perfusable channels within the constructs by using sacrificial materials. For example, Liu et al. [16] reported a multi-material bioprinting strategy using sacrificial ink to fabricate 3D centimeter-scale networks with perfusable channels, which supply the nutrients and oxygen to liver constructs.

To generate multiscale networks that meet the requirements for functional tissue culture, Kinstlinger et al. [38] successfully manufactured complex hierarchical channel networks by using sacrificial templates. Despite significant contributions to accelerating the manufacturing process and fabricating all-scale biomimetic hierarchical networks, the functionality of such networks for sustaining the *in vitro* tissue growth without channel collapse is yet to be proven [39].

Based on the demand for sustained *in vitro* tissue growth, Kolesky et al. [40,41] developed a method to fabricate a multichannel network using Pluronic F127 as the sacrificial material. A cell-laden tissue construct with >1cm thickness was established that could be perfused within a chip system for over 6 weeks. However, the complexity of such a network is insufficient to adequately facilitate versatile *in vitro* tissue culture.

Even though great progress has been made in the fabrication of perfusable channels with sacrificial materials, there is still a challenge to find a balance between the manufacturing scale, complexity of channel configuration, network long-term stability, and functional versatility.

Coaxial printing is another approach to achieve the goal of generating channel networks for *in vitro* tissue growth. To create 3D multichannel networks for sustained tissue constructs, Gao et al. [42] created 3D hydrogel-based vessel-like structures using pre-crosslinked hollow alginate filaments which were extruded through a coaxial nozzle. In another study, Gao et al. [43] utilized 3D coaxial cell printing to fabricate blood vessel-like structures using a hybrid bioink. However, the fabrication of intricate 3D multichannel networks with coaxial printing remains challenging.

Despite notable advancements in creating perfusable channels for *in vitro* models, a technological platform that would overcome the existing limitations, mostly related to the versatility in designs and multiscale fabrication, is yet to be developed. Moreover, achieving a sustained and controllable perfusion by using such 3D networks to enable the supply, exchange, and removal of products needed for the *in vitro* growth of a functional microtissue is yet to be explored and exploited.

In this study, we have explored the potential of 3D printing technology for the fabrication of multiple scales (from multi-millimeter scale down to micrometer scale) 3D channel networks with increasingly

complex designs, namely single-channel network (SCN), multichannel network (MCN), and dendritic network (DDN). In addition, we have incorporated pores along the channels with controllable size and spatial distributions. The effects of the main network characteristics on the diffusion of model substances throughout engineered hydrogel matrices were evaluated by contrast agent-enhanced micro-computed tomography (micro-CT) and confocal fluorescence microscopy in an attempt to establish a new platform for the design and fabrication of fit-for-purpose perfusable channel networks.

#### 2. Materials and methods

#### 2.1. Design of the channel networks

We designed three types of network structures, each tailored to represent specific functional requirements (Fig. 1a). The first type, SCN, is designed to quantitatively study the influence of network design parameters on diffusion processes. The second type denoted as MCN, features both inlet and outlet connections, enabling it to be seamlessly integrated with external tubes and pumps, thereby forming a closedloop system. This configuration permits controlled perfusion of the constructs. Additionally, the design allows for the adjustment of such parameters as the number of channels, their bending angles, and the size and number of pores on each channel to satisfy various design objectives, including a controlled spatial distribution of different bioactive agents in specific zones of the constructs. The third type, the DDN, encompasses a singular inlet and multiple outlets where each branch is equipped with a customizable number of pores, each with its own tailored dimensions. This design configuration is relevant for satisfying the diffusion requirements of an entire system, particularly within the context of larger-scale tissue constructs. The adaptability of this structure allows for the adjustment of branches and pores to optimize diffusion processes and deliver oxygen and nutrients to areas deep into the construct. All the designs were generated using computer-aided design (CAD) software and were additively manufactured as described below.

#### 2.2. Multiscale additive manufacturing of the networks

To fabricate the designed networks over different length scales, three different 3D printing methods (Fig. 1b) have been used, namely fused deposition modeling (FDM), stereolithography (SLA), and two-photon polymerization (2PP). The process began with the generation of STL format files from the CAD designs.

#### 2.2.1. FDM

Polylactic acid (PLA, UltiMaker PLA-green, 750 gr Natural with a filament diameter of 2.85 mm) was used for FDM printing. An Ultimaker 3 (UltiMaker B.V., The Netherlands) printer with a nozzle diameter of 0.25 mm was used to print the networks with a brim at the multimillimeter scale having a wall thickness of 0.50 mm, a channel diameter of 2 mm, and a layer thickness of 0.06 mm without support. Meanwhile, the infill density was set at 20 % and the printing bed temperature was 60 °C. We systematically varied the printing temperature from 210 °C to 220 °C and adjusted the printing speed from 9 to 30 mm/s to study how these variables influence the print quality. Upon finishing the printing process, the excess material was eliminated manually using a cutter and sandpaper. The specimens were then polished to a smooth finish with P500 sandpaper and finally cleaned in ethanol.

# 2.2.2. SLA

SLA was employed for the fabrication of the mm-scale networks. FormLab 3 (FormLabs Inc., Somerville, MA, USA) was used together with the "Clear" resin (FLGPCL04, FormLabs, USA). Designs in the STL format were subsequently sliced using the 3D printing slicer (Preform, Formlabs) to prepare the files for export to the FormLab 3 printer. We

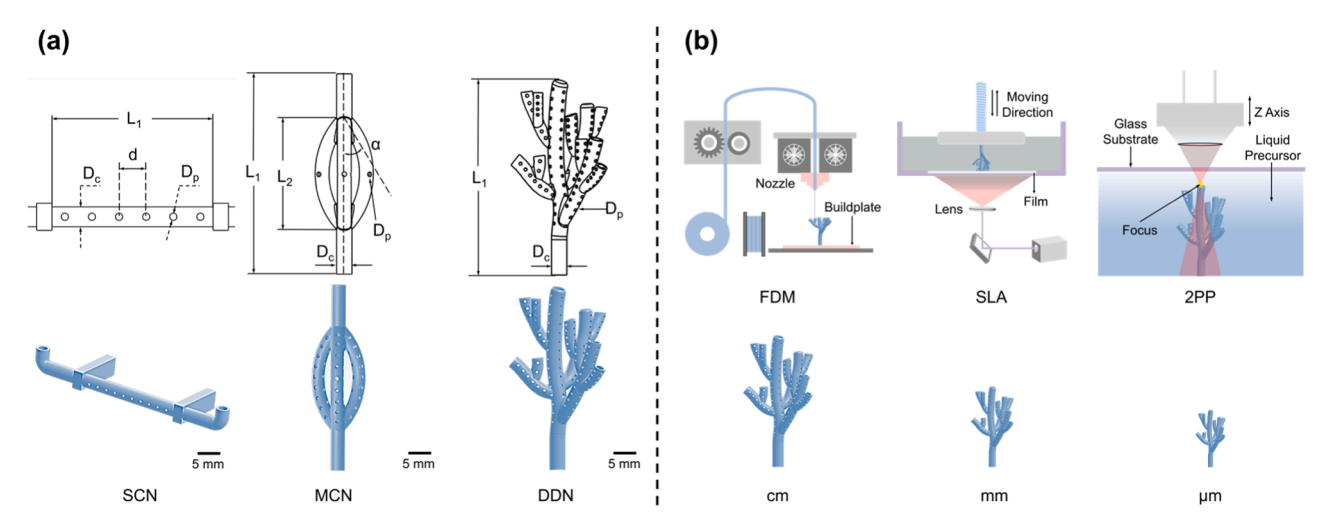


**Fig. 1.** (a) Design parameters and models of the three different networks: single-channel network (SCN), multiple-channel network (MCN), and dendritic network (DDN); (b) the 3D printing methods employed to fabricate the networks across multiple scales, ranging from multi-millimeter to micrometer dimensions. FDM = fused deposition modeling; SLA = stereolithography; 2PP = two-photon polymerization.

printed the SCNs and MCNs, with the same heights (i.e., 30 mm height in total) and a channel diameter of 2 mm under 5 different printing angles  $(0^{\circ}, 30^{\circ}, 45^{\circ}, 60^{\circ}, \text{ and } 90^{\circ})$  with a 50 µm layer thickness. Support structures were automatically generated in the Preform, with minor adjustments made to ensure proper adhesion to the surface of the specimens. Upon completing the printing process, all the specimens underwent a cleaning procedure using Formlabs Form Wash Machine (FormLabs Inc., Somerville, MA, USA) for 15 min, followed by immersion in fresh isopropanol for 10 min to thoroughly remove any residual resin from the surface. Then, a high-pressure air gun was used to clean both the surface of the specimens and the interior of the channels. This step was essential for removing any remaining resin or debris, thereby ensuring the cleanliness and integrity of the fabricated components, especially to ensure that the pores on the channel walls were open. Subsequently, the specimens were subjected to a curing process in Formlabs Form Cure Machine (FormLabs Inc., Somerville, MA, USA) for 20 min, at a temperature of 60 °C. Lastly, the support structures were removed using flush cutters, and the specimens were polished using P500 sandpaper.

### 2.2.3. 2PP

We used 2PP to fabricate microscale networks using a Photonic Professional GT machine (Nanoscribe, Eggenstein-Leopoldshafen, Germany) equipped with a femtosecond fiber laser (780 nm wavelength, 100 fs pulse duration, 80 MHz frequency). The IP-Q photoresist (Nanoscribe GMbH, Eggenstein-Leopoldshafen, Germany) was used for all the prints. The dip-in configuration (DiLL) and a  $10\times$  objective lens (NA = 0.3) were employed in the Galvo writing mode. Designs in the STL format were processed in Describe (Nanoscribe, Eggenstein-Leopoldshafen, Germany) to generate a GWL (general writing language) file.

Square silicon wafer substrates ( $25 \times 25 \times 0.725 \text{ mm}^3$ ) were cleaned with acetone (Sigma-Aldrich, Darmstadt, Germany) and isopropyl alcohol (IPA) (Sigma-Aldrich, Darmstadt, Germany), followed by activation with a 15-minute oxygen plasma treatment and silanization in a 2 % solution of 3-(trimethoxy silyl)propyl methacrylate (Sigma-Aldrich, Darmstadt, Germany) in ethanol. The substrates were then rinsed in acetone, demineralized water, and dried with compressed air. A droplet of IP-Q photoresist was deposited on the silanized silicon substrates. The fabrication parameters included a laser power (LP) of 45 mW and a scanning speed (v) of 100,000 µm/s, while the hatching distance (h) varied from 0.20 µm to 0.68 µm in 0.16 µm steps, and the slicing distance (s) varied from 0.5 µm to 3.2 µm in steps of 0.9 µm. Due to the size of the

structures exceeding the print field of the  $10 \times$  objective lens, they were split into hexagonal blocks ( $1000 \times 866 \times 301 \ \mu m^3$ ), which were oriented vertically. Following printing, the specimens were immersed in 1,2-propanediol monomethyl ether acetate (PGMEA) solution (Sigma-Aldrich, Darmstadt, Germany) for 25 min, followed by a 30-second immersion in a methoxy-nonafluorobutane  $C_4F_9OCH_3$  solution (Novec 7100, Sigma-Aldrich, Darmstadt, Germany). Finally, the specimens were dried by blow-drying with compressed air.

Each 2PP-printed network had 6 pores per channel and the designed pore diameter was 17  $\mu m$ . This compares to FDM and SLA printed networks which had 6 pores per channel with a design pore diameter of 800  $\mu m$ . After printing under various conditions, we compared the actual printed pore diameters with the designed sizes to evaluate the quality of the printed specimens. Therefore, three specimens were analyzed for each printing method, and two pores were randomly selected from each specimen for measurement. All the pore diameters were measured by using Image J (Image J, 1.54f) [44]. Each pore was measured 6 times, and the means and the corresponding standard deviations were considered for comparison.

#### 2.3. Diffusion experiments

# 2.3.1. Hydrogel printing to embed the channel networks

Sodium alginate powder (Thermo Fisher Scientific, Waltham, USA) was dissolved in  $0.9\,\%$  NaCl solution and stirred with a magnetic stirrer to form alginate hydrogel with concentrations of  $3.0\,\%$  and  $5.0\,\%$ . Subsequently, calcium chloride powder (CaCl $_2$ , Sigma Aldrich, Saint Louis, USA) was dissolved in distilled water to create a  $500\,\text{mM}$  CaCl $_2$  solution. 3D-printed boxes with perforated lids were fabricated to accommodate the networks and the hydrogel. The hydrogel was cast in the box containing the network using a syringe with a  $0.46\,\text{mm}$  nozzle diameter. The alginate layer had a thickness of  $10\,\text{mm}$ . The casting was performed from the bottom up until a fixed height to encapsulate the network and avoid the air bubbles. The box was then covered with the perforated lid and the CaCl $_2$  solution was added to crosslink the alginate *in situ*. Subsequently, the specimens were sealed and placed in a fridge until the diffusion tests.

# 2.3.2. Diffusion experiments

To visualize the diffusion process throughout the hydrogel matrix, a micro-CT scanner (Quantum FX®, Caliper, Canada) and an iodixanol-based contrast agent (1.320  $\pm$  0.001 g/ml, 60 % w/v, Stemcell Technologies, Germany) with a molecular weight of 1550.2 g/mol were used.

When delivering the contrast agent into the network, it was important to maintain a leakage-proof system. This was ensured by using two Eppendorf tubes connected to the network and sealing the connections with parafilm (Fig. 2a). The setup enabled a continuous supply of the contrast agent while preserving an appropriate atmospheric pressure to enable uninterrupted diffusion. It also eliminated the possible drying of the contrast agent during the tests. A support structure was used to maintain the specimen orientation inside the micro-CT machine to ensure proper alignment for the diffusion process. The field of view (FOV) was established at 40 mm  $\times$  40 mm, sufficient to image the specimen and to allow for a full view of all the parts of the setup relevant to analyzing the diffusion process. The tests were performed using a tube current of 180  $\mu A$  and a tube voltage of 90 kV, resulting in a specimen scan time of 2 min and a voxel size of  $78 \times 78 \times 78 \mu m^3$ . During the scanning of the specimen, the platform was rotated 360° to thoroughly examine the three-dimensional spatial distribution within the specimen. If the preview did not provide complete coverage, adjusting to a larger FOV or repositioning the specimen was necessary to ensure all the required data was acquired. After each micro-CT scan, the specimen was wrapped with parafilm and kept under a controlled humidity environment. This environment served the dual purpose of maintaining a consistent humidity of about 40 % and temperature levels around  $21\pm1$ °C, thereby preserving specimen integrity until the subsequent scan. We acquired images at  $t_0$  (before adding the contrast agent) and t = 2, 20, 60, and 90 min as well as t = 2, 3, 4, 5, 6, and 24 h. The diffusion experiments were performed by using the SCN networks printed by the SLA process because this process offered the best balance between resolution and scalability that enabled the fabrication of optimal final sample sizes needed for the diffusion experiments and the associated methodologies. The SCN networks were designed to capture the effects of the pore sizes (i.e., 0.8 mm and 1.6 mm), number of pores (i.e., 1 pore and 6 pores), and alginate concentration (i.e., 3 % and 5 %) on the

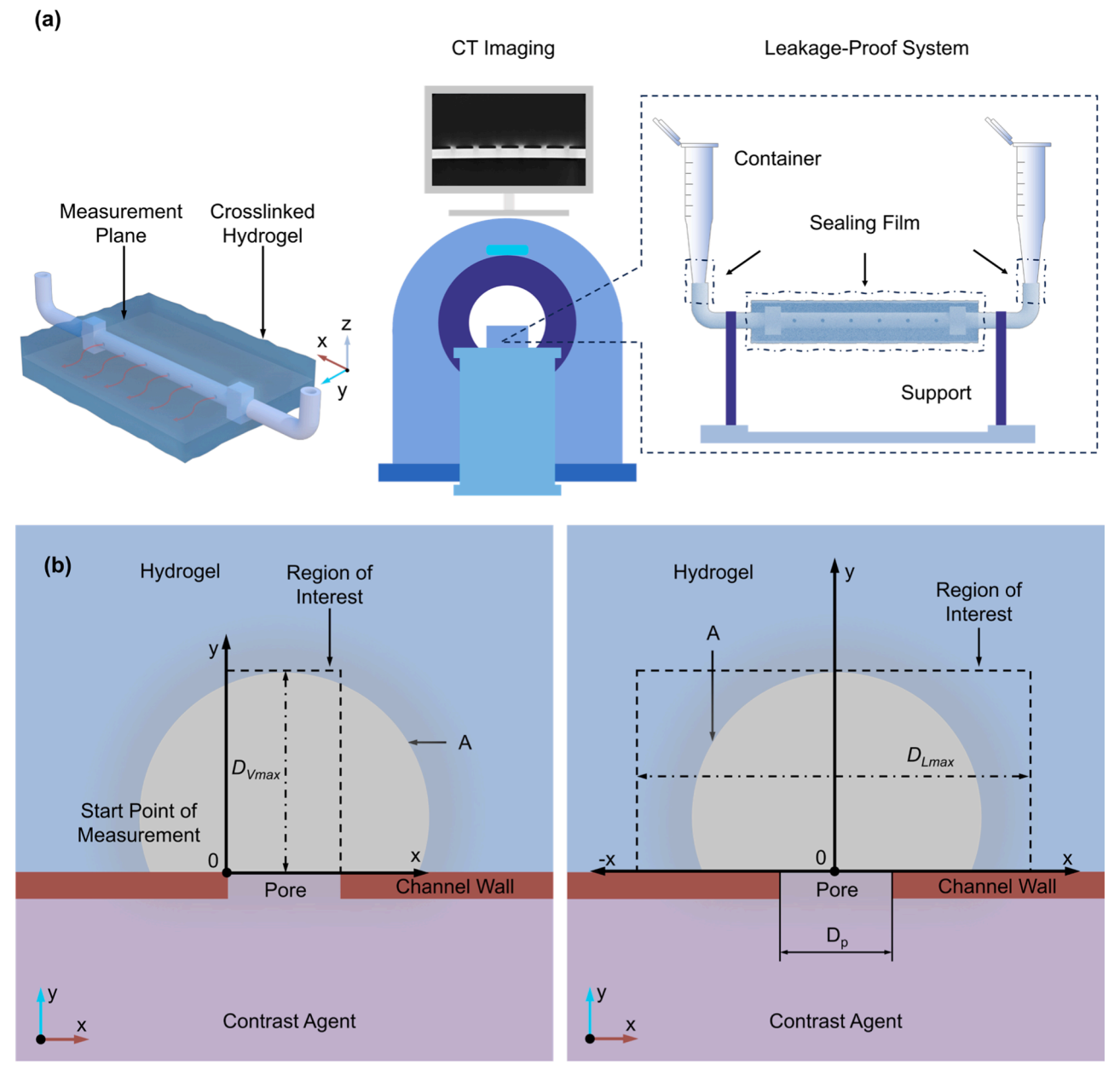


Fig. 2. (a) 3D printed SCN networks by SLA printing embedded in the alginate hydrogel matrix together with the leakage-proof setup used for the contrast agent-enhanced micro-CT experiments; (b) the measurement methods of the vertical and lateral diffusion distances. A = diffusion area;  $D_{Vmax} = \text{vertical largest diffusion}$  distance;  $D_{Lmax} = \text{lateral largest diffusion}$  distance;  $D_{Lmax} = \text{lateral largest diffusion}$  distance;  $D_{Lmax} = \text{lateral largest diffusion}$ 

diffusion of the contrast agent over time. Three specimens were tested for each set of experimental conditions. For each specimen tested, we recorded the gray values corresponding to the contrast agent present within the supply tube for calibration. The corresponding results were then used to calculate the mean values of the contrast agent concentration and to analyze the diffusion process with time.

#### 2.3.3. Image processing and data analysis

After image acquisition from micro-CT, all the stacks were exported to Image J (Image J, 1.54f) for processing. We chose a mid-sagittal slice of each specimen as the representative image at the middle of pores along the SCN to study the diffusion of the contrast agent into the hydrogel matrix. We set the unit of the experimental images to pixel, converted them to 8-bit, and then extracted the gray value (G) of the pixels in the images. We employed an experimentally validated linear relationship between the initial gray value of the alginate hydrogel at time t=0 and the gray value of the contrast agent, along with their respective concentrations:

$$C = kG + b \tag{1}$$

, where C is the normalized concentration of contrast agent within the hydrogel (% of contrast agent), G is the gray value (from 0 to 255), while k and b are constants.

The normalized concentration of the crosslinked alginate hydrogel  $(C_0)$  was considered 0 %, while the normalized concentration of the contrast agent  $(C_{max})$  was 100 %. We inserted the measured gray values of hydrogel and contrast agent into Eq. (1) to calculate k and b, which are specific to our experiments. This approach enabled the determination of the solute concentration within the crosslinked hydrogel at any diffusion time and distance when the gray value in such pixels was obtained

Subsequently, we applied two rectangular areas with different sizes as our region of interest (ROI) to measure the vertical and lateral diffusions within a specimen (Fig. 2b). During the vertical diffusion measurements, we assessed and determined the largest vertical diffusion distance (i.e., D<sub>Vmax</sub>), which was the distance from the pore to the farthest diffuse pixel that could be detected along the vertical direction. The measurement of this distance involves selecting the pixel located at the center of the pore and tracing along the vertical direction until reaching the last pixel, after which there are five consecutive pixels with a normalized concentration value of 0 %. Simultaneously, the average concentration of all the pixels along each transverse line segment spanning the pore diameter from the pore's initiation to the largest diffusion distance was gauged. In the case of lateral diffusion, we similarly gauged the largest lateral diffusion distance (i.e.,  $D_{Lmax}$ ) and calculated the average concentration value of all the pixels within each vertical line segment, using the pore as the center and the largest vertical diffusion distance as the measurement unit.

#### 2.3.4. Fitting to analytical solutions

For a detailed investigation of all the relevant parameters, we fitted a function obtained using analytical solutions to our experimental data to analyze the relationship between vertical diffusion distance, diffusion time, and solute concentration within the context of the underlying physics. We defined a function corresponding to the analytical solution of the 2D Fick's second law of diffusion for a semi-infinite boundary condition. This is derived from the standard mass diffusion equation (Crank, 1975) [45] as presented in (McOwen, 2003) [46] using the error function (*erfc*) and describes how a substance diffuses over time from a constant concentration boundary into a semi-infinite medium. For this semi-infinite boundary condition (*e.g.*, the initial concentration at the pore is fixed), the analytical solution can be written as:

$$C(x,t) = C_0 * \operatorname{erfc}\left(\frac{x}{2\sqrt{Dt}}\right)$$
 (2)

, where  $C_0$  is the initial concentration, erfc is Gauss complementary error function, D is the diffusion coefficient, x is the vertical diffusion distance, and t is diffusion time. This function was used as the fitting function for nonlinear curve fitting in Origin (2021, USA).

We plotted all groups of data to get scatter plots showing the contrast agent concentration along vertical diffusion distance at fixed time points, and then performed the fitted curve fitting for the relationship between vertical diffusion distance and contrast agent concentration using the following equation:

$$C(x) = C_0 * \operatorname{erfc}\left(\frac{x}{2 \times \sqrt{D_E t_{fixed}}}\right)$$
(3)

, where  $C_0$  is the initial concentration, erfc is the Gauss complementary error function,  $D_E$  is the equivalent diffusion coefficient, x is the vertical diffusion distance, and  $t_{fixed}$  is the fixed diffusion time.

#### 2.3.5. Statistical analysis

Origin (2021, USA) and Prism (10.2.3, GraphPad, US) were utilized for printing and diffusion results, including average pore sizes,  $D_{Vmax}$ , and diffusion area (i.e., A) to calculate the means, standard deviations, and p values. All the experiments were performed with at least three replicates. We performed a normality test using the Shapiro–Wilk test with alpha = 0.05 to confirm the normal distribution of the data in each group. We also performed a Student's t-test for the diffusion experiment focusing on a single parameter. We conducted an ordinary one-way ANOVA test, followed by post-hoc analysis using Tukey's multiple comparison test for comparing the means of more than two experimental groups. For all the analyses, a p-value < 0.05 was considered statistically significant.

#### 3. Results

#### 3.1. Fabrication efficiency

Based on the design considerations and optimization of the printing parameters, we successfully fabricated all three types of network designs (i.e., SCN, MCN, and DDN) employing the FDM, SLA, and 2PP printing techniques (Fig. 3). We could, therefore, realize the designed channel networks in a wide range of length scales from multi-millimeter to micrometer scales.

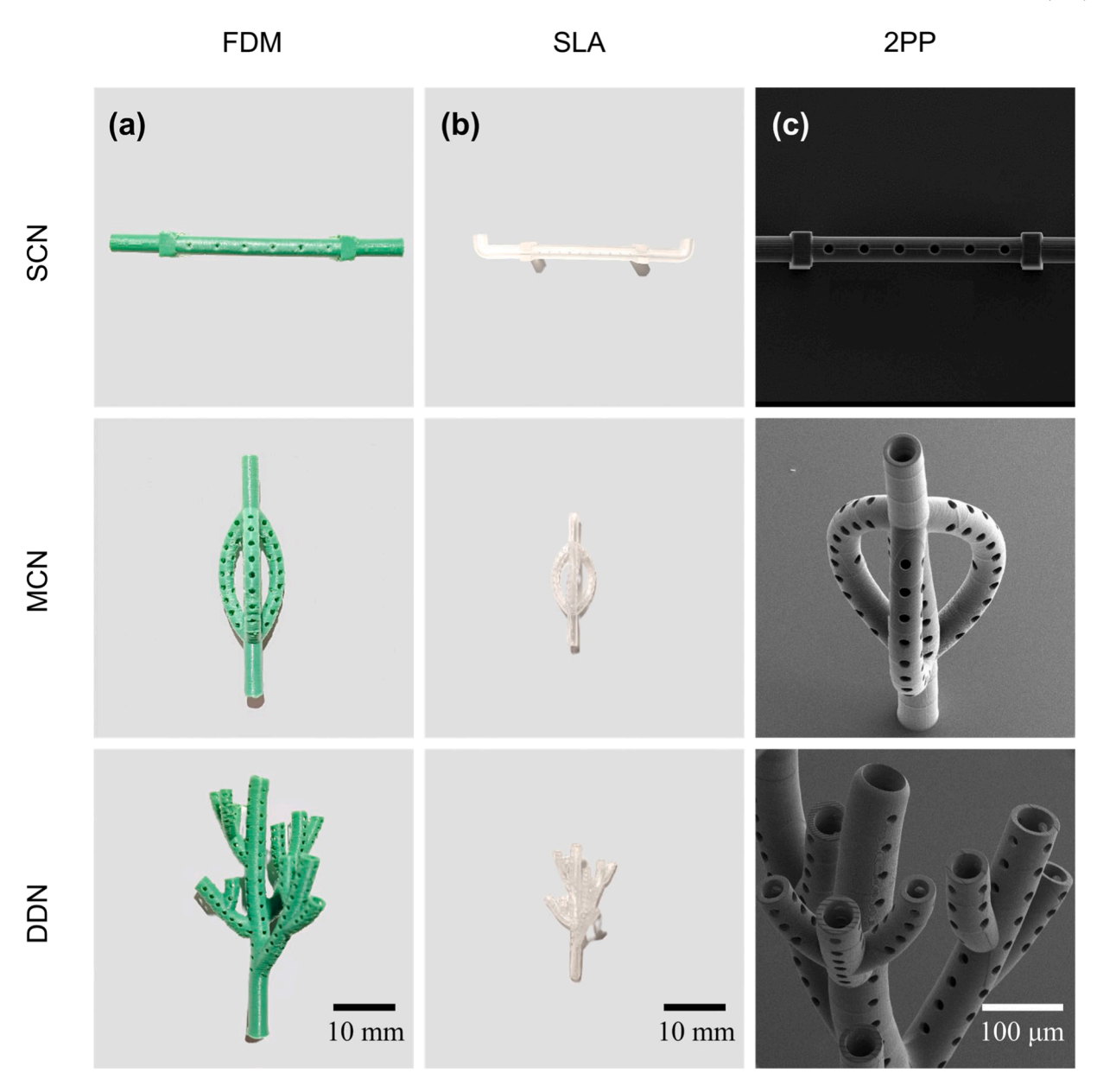
#### 3.1.1. FDM

We systematically studied the effects of the printing speed and printing temperature on the shape, size, and reproducibility of the different PLA networks, which allowed us to identify the optimum FDM printing conditions.

At low temperatures (*i.e.*,  $T=210-213~^{\circ}$ C), the networks collapsed when printing at low speeds (*i.e.*, <9 mm/s) whereas uneven pore diameters were observed when printing at high speeds (*i.e.*, over 21 mm/s) (Fig. 4a). For temperatures between 213 and 216  $^{\circ}$ C, the printed specimens exhibited very good shape fidelity over a large range of printing speeds. However, higher temperatures (*i.e.*,  $T>216~^{\circ}$ C) resulted in excessive melting of the PLA filament, leading to collapsed structures at low printing speeds and significant residue or strings on the surface of the specimens at high printing speeds necessitating thorough cleaning.

Within the range of the studied printing temperatures, it was observed that printing reproducibility was notably enhanced for a printing temperature of  $215\,^{\circ}\text{C}$ . Consequently, this temperature was selected as the optimal printing temperature used for the subsequent experiments. At this printing temperature, the effects of printing speeds between 9 and 21 mm/s on network shape fidelity and pore sizes were systematically investigated (Fig. 4b).

The results indicated that the printed pore diameter at a speed of 9 mm/s closely approximated the original design size of 800  $\mu$ m (i.e., 780



 $\textbf{Fig. 3.} \ \ \textbf{The 3D networks printed with the optimal conditions by using FDM, SLA, and 2PP methods.}$ 

 $\pm$  67 µm). However, the relatively large standard deviation of the pore size suggested poor reproducibility. Among the remaining printing speeds, 15 mm/s exhibited a relatively smaller standard deviation of pore size and maintained an acceptable average pore size of 830  $\pm$  35 µm, rendering it a more favorable option as it balances geometrical fidelity with reproducibility, as compared to the pore sizes of 870  $\pm$  27 µm, 880  $\pm$  18 µm, and 860  $\pm$  97 µm at 12, 18, and 21 mm/s, respectively. These findings underscored the critical interplay between printing temperature and speed in achieving optimal print quality. Therefore, for a printing temperature of 215 °C, a printing speed of 15 mm/s was expected to balance the competing requirements of geometrical fidelity, reproducibility, and manufacturing speed. Under these printing conditions, networks featuring all the designed parameters could be successfully printed by FDM.

# 3.1.2. SLA

In the case of SLA printing, the orientation of the network allows for the adjustment of both printing time and pore diameter. Therefore, the effects of printing angles from  $0^\circ$  to  $90^\circ$  on the pore sizes and printing

time were evaluated for SCN and MCN (Fig. 4c).

The largest deviations from the designed pore sizes were observed when the specimens were oriented at  $0^\circ$  and  $90^\circ$  for both SCN and MCN. The average pore size of the SCN was  $820\pm32~\mu m$  and  $780\pm32~\mu m$  at  $0^\circ$  and  $90^\circ$ , while that of MCN was  $800\pm36~\mu m$  and  $810\pm45~\mu m$ . Notably, orientations of  $30^\circ$ ,  $45^\circ$ , and  $60^\circ$  exhibited better shape fidelity compared to the printing results at  $0^\circ$  and  $90^\circ$ . For example, the pore sizes of the SCN were, respectively,  $800\pm9~\mu m$ ,  $810\pm13~\mu m$ , and  $790\pm3~\mu m$  for the printing angles of  $30^\circ$ ,  $45^\circ$  and  $60^\circ$ , while those of MCN were  $800\pm7~\mu m$ ,  $810\pm13~\mu m$  and  $800\pm32~\mu m$  for the same printing angles (Fig. 4c). Despite the longer printing time associated with a  $30^\circ$  orientation (around 130 and 220 min for SCN and MCN, respectively), the relatively small standard deviation of its printed pore sizes (i.e., 09 and 7  $\mu m$  in both networks) suggested it was the most suitable choice among the orientations considered.

#### 3.1.3. 2PP

In this case, we used a 17  $\mu m$  pore as the original design size and measured the pore sizes of the SCN specimens printed under different

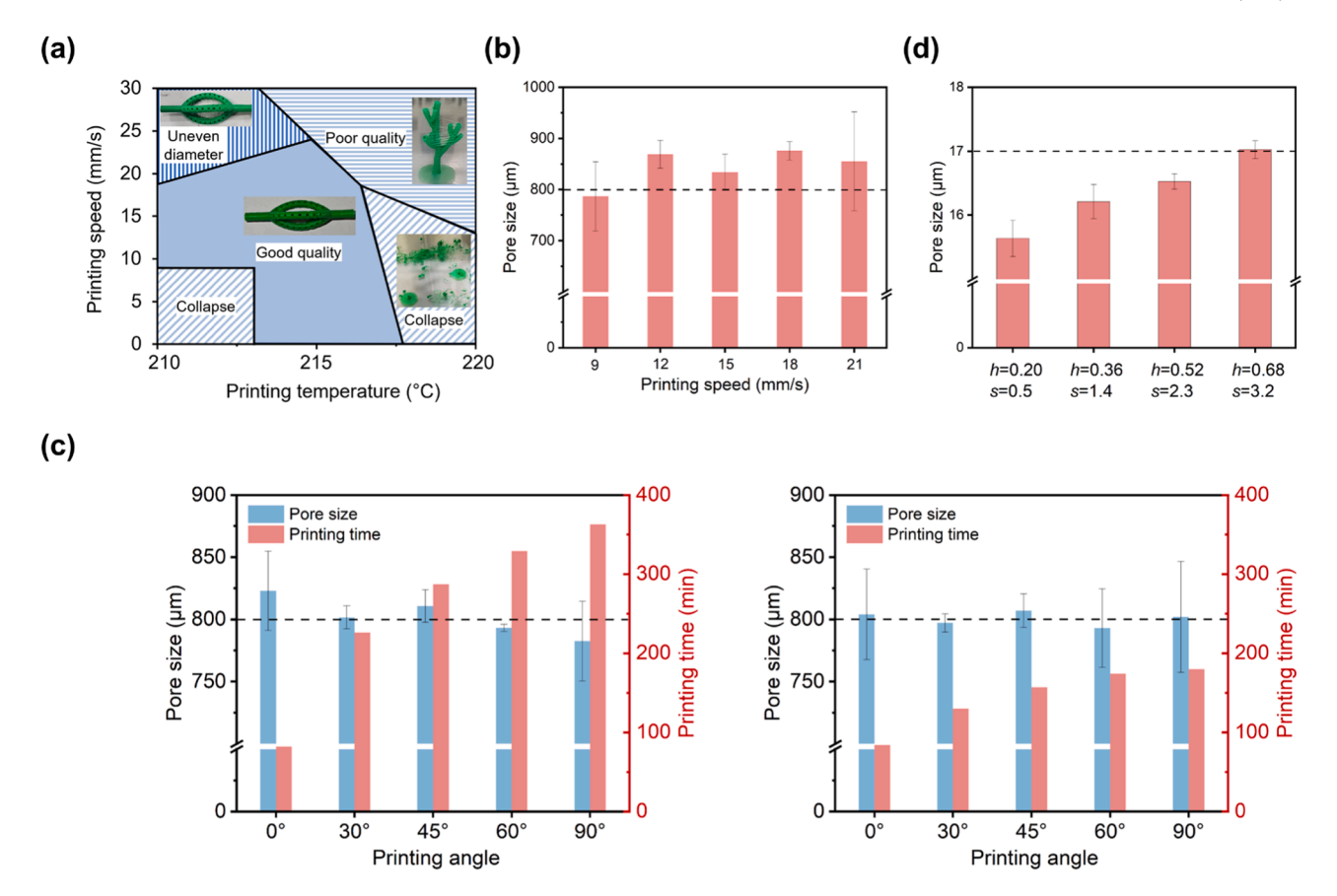


**Fig. 4.** (a) Effects of printing temperature and printing speed on the shape and size fidelity of the networks printed using FDM; (b) effects of printing speed on the pore size of the SCN and MCN networks printed by FDM (printing temperature T = 215 °C); (c) effects of printing angle on the pore size of the SCN networks printed by SLA; (d) effects of hatching distance (h) and slicing distance (s) on the pore size of the SCN networks printed by 2PP. Three samples were selected for each condition, while 2 pores were chosen, and each pore was measured 6 times.

hatching and slicing distances (Fig. 4d). Overall, the structures exhibited high fidelity to the original design dimensions, especially when the hatching distance was h = 0.20 um and the slicing distance was s = 0.50μm. More specifically, the pore size measurements of the printed networks in this condition were remarkably close to the intended 17  $\mu m$ diameter, displaying an average pore size of 17.0  $\pm$  0.1  $\mu$ m. When the hatching distance was 0.36 and 0.52 µm, and the slicing distance was 1.40 and 2.30 µm, the pore size had less accuracy as compared to the designed size with an average pore size 16.5  $\pm$  0.1 and 16.2  $\pm$  0.3  $\mu$ m, respectively. However, the pore size was 15.6  $\pm$  0.3  $\mu m$  with 0.68  $\mu m$ hatching distance and 3.20 µm slicing distance, which had a larger deviation as compared to the designed size. These values demonstrated, as expected, that the specimens printed using 2PP exhibited superior dimensional accuracy as compared to those fabricated using FDM and SLA methods, with significantly lower standard deviations that indicated enhanced reproducibility.

Further insights into the findings related to network shape fidelity after printing revealed some size differences between individual pores measured along the network channel. Therefore, we selected the specimens printed by using the best conditions for each printing method and compared the diameters of pore 1 and pore 2 (Table S1). The results indicated that the 2PP printed specimens exhibited the smallest size difference between the two pores, with only a 0.29 % deviation from the designed size of 17  $\mu m$ . In contrast, the FDM and SLA specimens showed 0.42 and 0.71 % deviations, respectively, relative to the original pore size of 800  $\mu m$ . Although the difference between both pores of the FDM specimens was smaller than that of the SLA specimens, the variation in size within the individual pores of the FDM specimens was greater, indicating less consistency.

#### 3.2. Diffusion experiments

Following the diffusion experiments, we performed 3D reconstructions of the contrast agent-enhanced micro-CT images of all the specimens (Video S1), to visualize the diffusion within the constructs. In the layer-by-layer reconstruction, we selected the cross-section of the center of the SCN channel as a reference surface to study the effects of various parameters on diffusion. 2D projections were used for quantification of the results (Figure S1).

#### 3.2.1. Effects of the pore size

For these experiments, SCNs with one pore of either 0.8 mm or 1.6 mm were used. The hydrogel concentration was 3.0 % and the test duration was 6 h (*i.e.*, 0.8 mm-3 %-1 pore-6 h and 1.6 mm-3 %-1 pore-6 h).

After 6 h of diffusion, the results indicated that the diffusion area corresponding to the 1.6 mm pore was larger than that of the 0.8 mm pore (Fig. 5a). Quantification of the largest diffusion distance in both vertical and lateral directions showed a vertical diffusion distance of 3.3  $\pm$  0.2 mm for the 0.8 mm pore vs. a vertical diffusion distance of 3.9  $\pm$  0.2 mm for the 1.6 mm pore (Fig. 5b). In the lateral direction, the 0.8 mm pore resulted in a total diffusion distance of 5.4  $\pm$  0.2 mm vs. 6.6  $\pm$  0.2 mm in the case of the 1.6 mm pore.

The profiles of the diffused contrast agent concentrations indicated the largest gradients closest to the pore (within 1 mm distance from the pore center) in both directions (Fig. 5c). In addition, the distribution of the contrast agent concentration within the diffusion area also showed differences between the small and the large pores. For the pore size of 0.8 mm, the normalized concentration decreased along the vertical

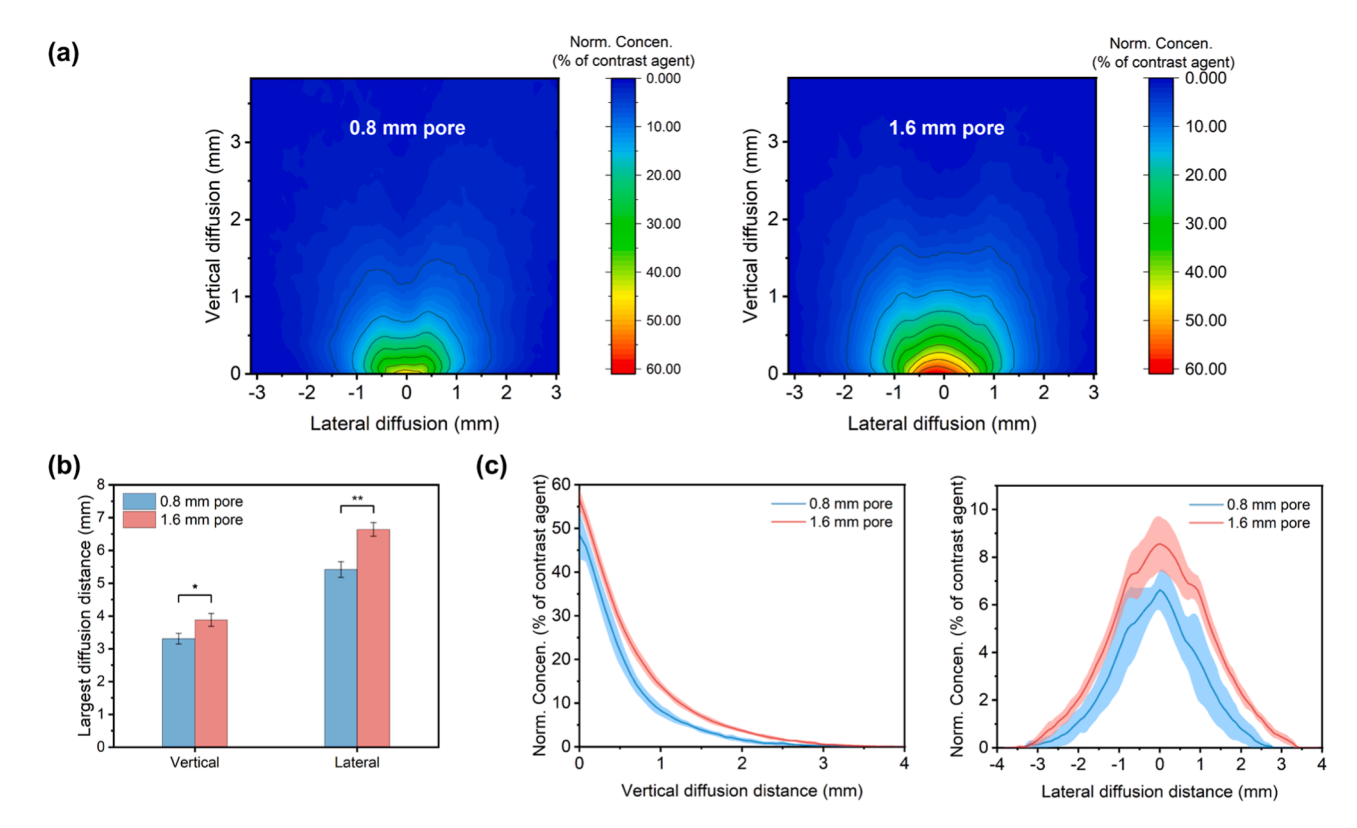


**Fig. 5.** Effects of pore size on (a) diffusion area; (b) largest diffusion distance in the vertical and lateral directions, and (c) normalized concentration profile in the vertical and lateral directions after 6-hour diffusion, respectively. The data (n=3) are expressed as mean  $\pm$  standard deviation (SD). Statistical significance is denoted by \*, \*\*, corresponding to p-value < 0.05, and p-value < 0.01.

distance from above 47 % closest to the pore (highest values in the middle) to 0.09 % further away from the pore (at the maximum vertical diffusion distance). For the pore size of 1.6 mm, the normalized concentration varied between 55 % and 0.10 % along the same distance.

#### 3.2.2. Effects of the number of pores

In this section, SCN with single pore or six pores with a pore diameter of 1.6 mm were used. The hydrogel concentration was 3.0 % and the test duration was 6 h. (*i.e.*, 1.6 mm-3 %-1 pore-6 h and 1.6 mm-3 %-6 pores-6 h).

After 6 h of diffusion, the diffusion distance and diffusion area of the single-pore specimens were smaller than the average values observed in the 6-pore specimens (Fig. 6a). More specifically, quantification of the largest diffusion distance in the vertical directions showed a vertical distance of  $3.9\pm0.2$  mm for the single pore specimens vs. a vertical distance of  $6.2\pm0.2$  mm for the 6-pore specimens. Meanwhile, single-pore specimens resulted in a total area of  $24.1\pm0.8$  mm $^2$  vs.  $31.9\pm0.7$  mm $^2$  in the case of the 6-pore specimens as shown in Fig. 6b. From a single to a 6-pore configuration, a 32 % increase in the concentration of the contrast agent within the diffusion area was observed after 6-hour diffusion.

The distribution of the contrast agent within the diffusion area also showed differences between the specimens with different pore numbers (Fig. 6c). For the 6-pores specimens, the normalized concentration decreased along the vertical distance from above  $63\,\%$  closest to the pore (highest values in the middle) to  $0.11\,\%$  further away from the pore (at the maximum vertical diffusion distance). For the 1 pore specimens, the normalized concentration varied between  $55\,\%$  and  $0.10\,\%$  along the same distance.

#### 3.2.3. Effects of alginate concentration

Following 6 h of diffusion of the contrast agent through a pore of 0.8 mm SCN into alginate hydrogels of 5 % and 3 % (i.e., 0.8 mm-5 %–1

pore-6 h and 0.8 mm-3 %-1 pore-6 h), slight differences were observed regarding the diffusion area and distance in both diffusion distance and diffusion area between the 5 % and 3 % alginate hydrogel specimens (Fig. 7a). Specifically, quantification of the largest diffusion distance in the vertical direction resulted in a vertical distance of  $2.9 \pm 0.2$  mm for the 5 % alginate hydrogel specimens as compared to  $3.3 \pm 0.2$  mm for the 3 % alginate hydrogel specimens. Additionally, the total lateral diffusion distance was  $4.8 \pm 0.3$  mm for the 5 % alginate hydrogel specimens vs.  $5.4 \pm 0.2$  mm for the 3 % alginate hydrogel specimens (Fig. 7b).

Furthermore, both in the 5 % and 3 % alginate hydrogel specimens, the normalized solute concentration exhibited the same trend (Fig. 7c), decreasing along the vertical distance from approximately 47 % in the pore vicinity (with the highest values at the center) to 0.09 % further from the pore (at the largest vertical diffusion distance). At the same time, the normalized solute concentration of the 5 % alginate hydrogel specimens was slightly smaller than that of the 3 % alginate hydrogel specimens for any given diffusion distance.

# 3.2.4. Effects of diffusion time

Extending the diffusion time from 6 h to 24 h, under otherwise similar conditions (i.e., 3 % alginate hydrogel, 1.6 mm pore, and 1 pore configuration, 1.6 mm-3 %-1 pore-6 h and 1.6 mm-3 %-1 pore-24 h) resulted in longer-term diffusion profiles (Fig. 8a). In contrast to the minor differences observed between superficial and middle-range areas, the 24-hour diffusion of the contrast agent resulted in an increased diffusion distance and area as compared to the diffusion experiments performed for only 6 h (Fig. 8a, b).

More specifically, the vertical diffusion distance increased from 3.9  $\pm$  0.2 mm to 6.8  $\pm$  0.3 mm, and the lateral diffusion distance from 6.6  $\pm$  0.2 mm to 11.5  $\pm$  0.7 mm as the diffusion time increased from 6 h to 24 h diffusion, respectively.

The distribution of the contrast agent concentration within the

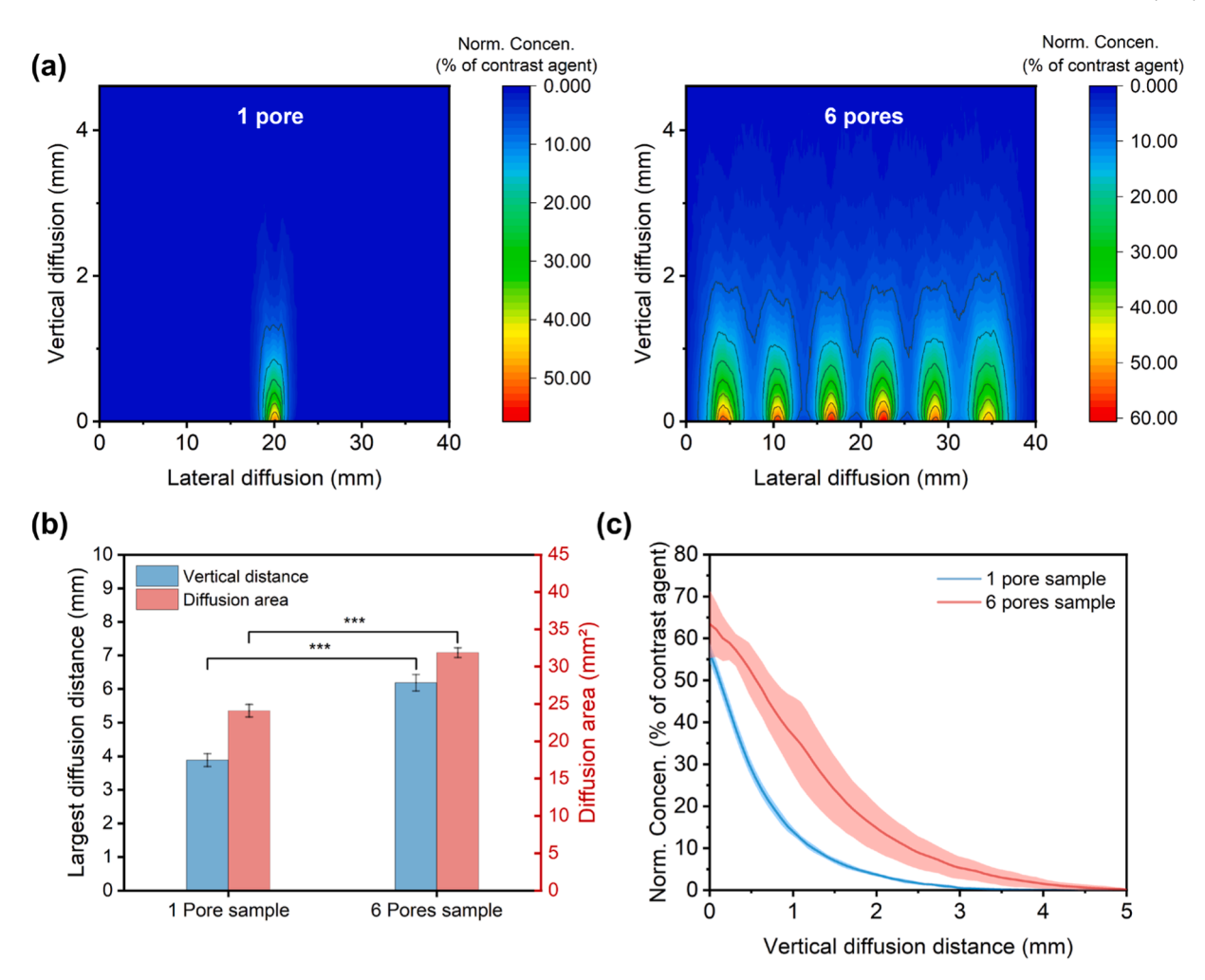


**Fig. 6.** Effects of pore number on (a) diffusion area; (b) largest diffusion distance in the vertical and lateral directions, and (c) normalized concentration profile in the vertical and lateral directions after 6-hour diffusion, respectively. The data (n=3) are expressed as mean  $\pm$  standard deviation (SD). Statistical significance is denoted by \*\*\*, corresponding to *p-value* < 0.001.

diffusion area also showed differences between the 6 h and 24 h diffusion specimens (Fig. 8c). For the 6 h specimens, the normalized concentration decreased along the vertical distance from >55 % closest to the pore (highest values in the middle) to 0.10 % further away from the pore (at the largest vertical diffusion distance,  $3.9\pm0.2$  mm). For the 24 h specimens, the normalized concentration varied between 60 % and 0.09 % along the same direction.

A second model system consisting of gelatin/glucose, was also investigated (Figure S4) and the results demonstrated the suitability of the proposed platform for studying clinically relevant compounds, and its adaptability to different assessment methods, such as  $\mu CT$  and fluorescence confocal microscopy, which are frequently used in tissue engineering and regenerative medicine.

# 3.2.5. Comparison of all the parameters

Histograms of the largest vertical and lateral diffusion distances of the specimens with all the parameter combinations were also generated to more intuitively observe and compare the impact of each parameter on the diffusion behavior (Figs. 9a and b). As it was clear from this comparison, the largest vertical and lateral diffusion distances for the 3% hydrogel specimens were 13.4% greater distances relative to the 5% concentration hydrogel specimens. As for the effects of the pore size, the largest vertical and lateral diffusion distances increased by 17.3% and 22.6%, respectively, for the 1.6 mm pore as compared to the 0.8 mm ones. Regarding the effects of the number of pores, the largest vertical diffusion distance of the 6-pore specimens increased by 59.5% as

compared to the 1-pore specimens. Finally, the maximum vertical and lateral diffusion distances of the specimens that diffused for 24 h rose by 72.9 % and 76.1 %, respectively, compared to the specimens that diffused for 6 h. Each group of specimens with different parameter combinations had a similar improvement in vertical and lateral diffusion distances, which further proved the validity of the experiments and the reliability of the data.

#### 3.2.6. Results of curve fitting to the analytical solution

The goodness of fit was evaluated using the coefficient of determination ( $R^2$ ) and root mean square error (RMSE) (Table 1). In addition, the equivalent diffusion coefficient  $D_E$  was calculated to quantify the diffusion ability of the designed specimens (Table 1). The  $R^2$  values of the four groups ranged between 0.91 and 0.95, while RMSE ranged between 0.07 and 0.08 mm<sup>2</sup>/s, which indicated the goodness of fitting. Moreover, an average  $D_E$  was also calculated from 1.5 h to 6 h (Fig. 9d). This fitting was consistent with the basic principles of Brownian motion and Fick's laws of diffusion governing the relationship between contrast agent concentration and diffusion distance in a 2D diffusion process at fixed diffusion time points.

# 4. Discussion

Clinically relevant 3D *in vitro* models are in great demand for disease modeling, drug screening, tissue engineering, and regenerative medicine [3,4]. Nevertheless, limitations related to biofabrication and

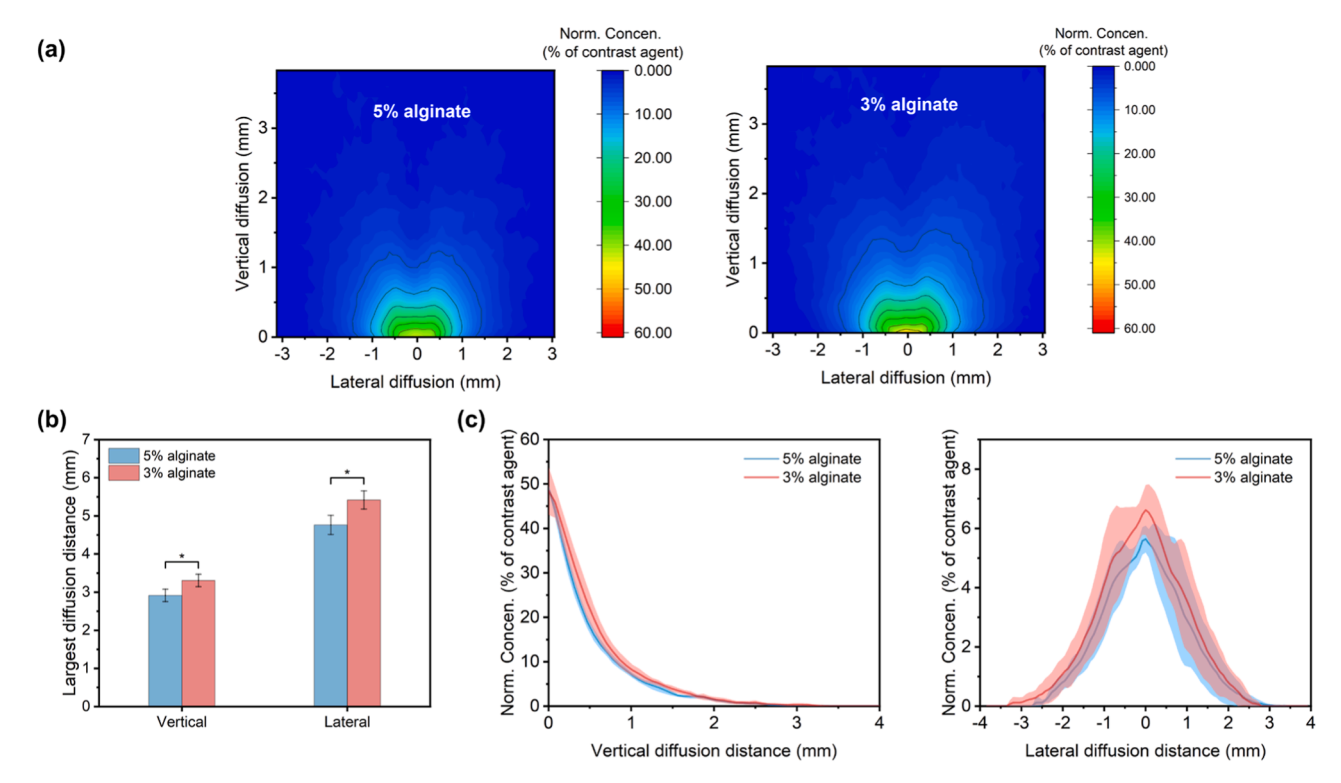


Fig. 7. Effects of hydrogel concentration on: (a) diffusion area; (b) largest diffusion distance in vertical and lateral directions, and (c) normalized concentration profile in the vertical and lateral directions after 6-hour diffusion, respectively. The data (n=3) are expressed as mean  $\pm$  standard deviation (SD). Statistical significance is denoted by \*, corresponding to p-value < 0.05.

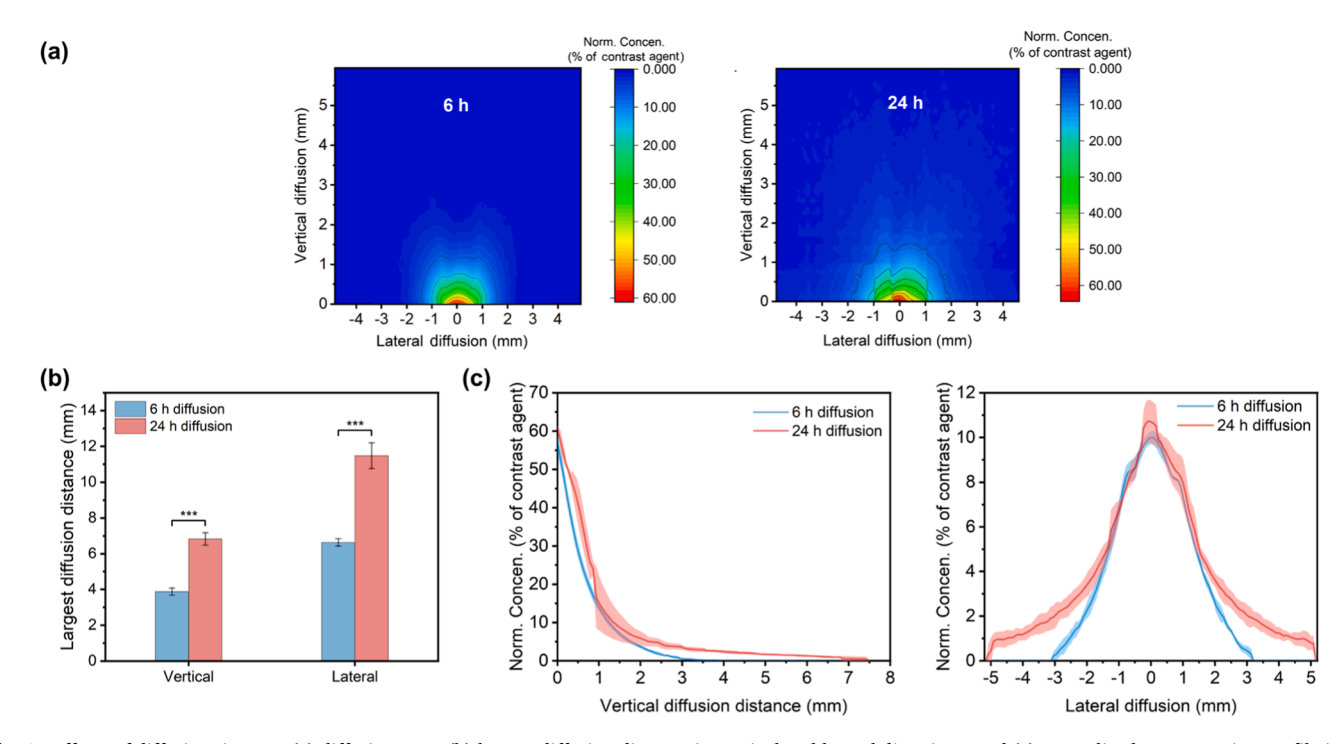


Fig. 8. Effects of diffusion time on: (a) diffusion area; (b) largest diffusion distance in vertical and lateral directions, and (c) normalized concentration profile in the vertical and lateral directions after 6-hour diffusion, respectively. The data (n=3) are expressed as mean  $\pm$  standard deviation (SD). Statistical significance is denoted by \*\*\*, corresponding to *p-value* < 0.001.

diffusion of needed factors to sustain tissue growth make the scale-up of such models very challenging [47].

In this study, by leveraging multiple 3D printing technologies, perfusable 3D channel networks with controlled porosity and increasingly complex geometries were successfully fabricated at various length scales. These networks can be incorporated into constructs to form a platform for the supply of oxygen and nutrients and the removal of metabolic byproducts during *in vitro* tissue growth. Such a platform has

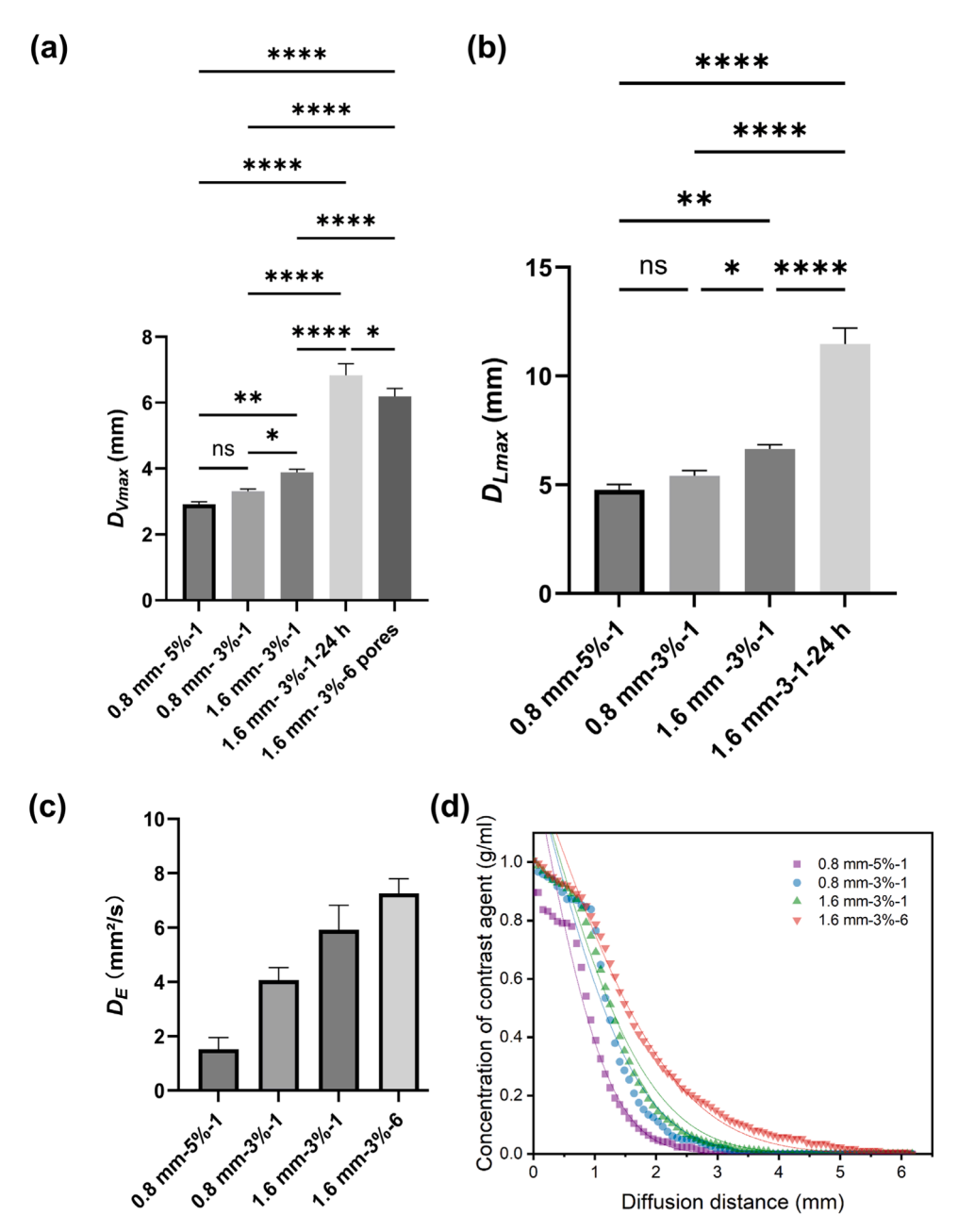


Fig. 9. The vertical (a) and lateral (b) diffusion distances of all the experimental groups; (c) the equivalent diffusion coefficient  $D_E$  of all groups; (d) curve fitting of all groups for 6 h diffusion. The data (n=3) are expressed as mean  $\pm$  standard deviation (SD). Statistical significance is denoted by \*, \*\*, \*\*\*, \*\*\*\* corresponding to p-value < 0.05, p-value < 0.01, p-value < 0.001, p-value < 0.001 respectively. The non-asterisks indicated that the differences between the groups are not statistically significant (*i.e.*, p-value > 0.05).

**Table 1**Results of fitting curves to the analytical solution.

Parameters	1.6 mm-3	1.6 mm-3	0.8 mm-3	0.8 mm-5
	%-6	%-1	%-1	%-1
R-square RMSE (mm <sup>2</sup> /s) $D_E (\times 10^{-5})$ (mm <sup>2</sup> /s)	$0.96$ $0.071$ $7.2 \pm 0.3$	$0.96 \\ 0.072 \\ 4.8 \pm 0.2$	0.95 0.080 $3.9 \pm 0.2$	$0.92 \\ 0.082 \\ 2.1 \pm 0.1$

great versatility in terms of design and scalability showing great potential for the establishment of an integrated technology that enables the development of superior 3D *in vitro* models for various applications. In addition, the proposed platform provides additional possibilities to tailor and control the biofunctionalities of the 3D *in vitro* tissue model for

any given application, which go beyond those offered by the existing models [16,38,40–42] (e.g., diffusion properties and spatial control of the diffused factors or supplied cells).

# 4.1. Multiscale printing of the porous 3D networks

Each printing method used for the fabrication of the porous networks has its own advantages and limitations (Table 2). The printing conditions were optimized for each method to achieve the best geometric fidelity for each network design. In the case of FDM printing, the collapse of the networks when applying higher temperatures or lower printing speeds can be due to a too-low channel wall thickness. If the number of printed layers of the channel wall is <2 (i.e., the wall thickness is <0.5 mm), the material can start to deform, affecting the stability of the printed structure. Therefore, ensuring that each printed channel

**Table 2**Comparison of the three printing techniques used to produce the porous networks.

Characteristic/ Method	FDM	SLA	2PP
General [48]			
Resolution	>50 μm	>25 μm	$\sim 1~\mu m$
Scalability	Highly scalable	Limited scalability	Poor scalability
Material compatibility	Wide range of materials	Limited to photopolymer resins	Limited to specialized photosensitive resins
Cost	Low, widely available equipment	Cost-effective	High; expensive equipment
Specific to the study			
Channel pore size	>800 µm	400 to ~1000 μm	<400 μm
Network design complexity	Moderate; Large networks but limited resolution for small features (< 400 µm)	Moderate	High; Complex designs but small networks
Channel wall thickness	Thick (>0.5 mm)	Moderate (>0.3 mm)	Thin ( $< 100 \ \mu m$ )

includes a minimum of a two-layer wall was necessary, with a three-layer wall being the most optimal configuration. This approach guaranteed that the walls of the printed structure remained robust, preventing deformation or collapse caused by excessively thin walls.

In the case of SLA printing, optimizing the printing angle was important because it significantly influenced both the network shape fidelity and the printing time (Fig. 4b). Because the network is printed layer by layer, varying the printing angle results in different numbers of layers needed to print each pore. This variation contributes to pore size accuracy, as more layers typically introduce a higher potential for errors. This can explain why compared to a printing angle of 30°, the specimens printed at 0° and 90° exhibited larger standard deviations, with individual specimens deviating significantly from the designed size of 800  $\mu m$ . Furthermore, when the printing angle was 90°, there was enough support and adhesion for printing the bottom half of the pore. However, some unevenness or even slight deformation is expected while printing the upper half of the pore due to the lack of particularly good support (Figure S2). These findings highlight the need to check the sizes of all the pores incorporated into a specimen when evaluating its geometric fidelity, particularly in the case of FDM and SLA methods that rely on layer-by-layer printing.

In FDM and SLA layer-by-layer printing, the first layer is often the one with the highest printing accuracy and good adhesion. However, as the number of printed layers increases, there is a considerable probability that subsequent layers will not maintain the same accuracy. This may result in a slightly different diameter between the first printed pore and the last printed pore on the same specimen.

For the 2PP, the pore size fidelity of the 2PP-printed specimens was highly accurate. As the hatching and slicing distances increased, the pore sizes deviated more from the intended 17  $\mu m$ , but still exhibited greater accuracy and reproducibility than those printed using FDM and SLA methods. However, due to the relatively small size of 2PP-printed specimens, manually handling them and conducting diffusion experiments remains a challenge.

The networks proposed in this study are designed to study the *in vitro* growth and functions of microtissues under pathophysiological conditions. In practice, the manufacturing processes used to create the multiscale porous networks can be upscaled to different extents, provided that the optimum design for a specific tissue is established. For example, while 2PP offers capabilities for fabricating intricate networks with high resolution, its scalability could be achieved by integrating automation

(such as automated print removal and reload), allowing for the fabrication of multiple structures in the same print. For the stereolithography process suited for larger structures than 2PP, scalability could be achieved by using larger printing plates. In addition, automation of cleaning and curing steps would enable high-volume production. The FDM process benefits from relatively lower costs and wider accessibility. Scalability for this method can be addressed by enlarging the printing plates or by using parallel printing modules. With the build plates of the FDM printers used in our study (20  $\times$  20 cm), 20 networks could be printed in one run, taking up to 12 h.

#### 4.2. Effects of network features and hydrogel concentration on diffusion

Despite the many studies focused on the incorporation of perfusable channels within hydrogels [42,43], a physics-based understanding of the diffusion processes is lacking. We used contrast agent-enhanced micro-CT and analytic solutions of Fick's equation to elucidate the physics of the diffusion process governing the function of such perfusable networks. This is important because the diffusion of any molecule (including the contrast agent) through a porous channel network into a hydrogel matrix is influenced by multiple factors. These include the channel diameter, pore diameter, the number of pores, the size of the molecule, and hydrogel attributes.

#### 4.2.1. Effects of network features on diffusion

Among the different network parameters investigated here, the number of pores had the most prominent effect on the diffusion area. By adjusting the distance between the pores, one can optimize the diffusion distances according to the requirements of a particular application. Furthermore, by adjusting the pore size and the number of pores, the porous network can provide more controllable and customizable functions compared to the non-porous network.

Meanwhile, the highest solute concentration diffusing through the pore can only reach around 55 % (Fig. 6c) because each measurement covered the average concentration of all the pixels on a line segment of a certain length (*i.e.*, largest vertical diffusion distances of each group). The concentration in the middle of this measurement segment was higher (*e.g.*, 85.18 %), while the concentration at both ends was lower (*e.g.*, 0.10 %), resulting in a mean value of 45–65 % after averaging.

### 4.2.2. Effects of hydrogel concentration on diffusion

It is noteworthy that the 5 % alginate hydrogel specimens were found to exhibit a slower initial diffusion rate than that of the 3 % alginate hydrogel specimens (Fig. 9d). That is because the diffusivity of a hydrogel system depends on the number of physical or chemical cross-linking sites per unit volume in the hydrogel polymer network [49,50]. For the same volume, a hydrogel with a higher concentration contains more crosslinking sites, resulting in a smaller pore size (around 60 nm) within the hydrogel mesh [51]. A higher alginate concentration will, thus, lead to the diffusing molecules having more difficulty penetrating the hydrogel mesh and diffusing.

# 4.2.3. Effects of time on diffusion

Considering the curves of different time points (Figure S3), we found that the fitted curves deviated more from the experimental data points for the diffusion times 2, 20, and 60 min. This could be caused by the hydrogel attempting to enter the pores to different extents, causing the diffusion distance and solute concentration of each specimen to be initially more variable. This situation disappeared after 60 min, as indicated by the more stable values of the equivalent diffusion coefficient  $D_E$ .

Furthermore, during the curve fitting process, we found that the  $D_E$  of two groups of specimens (i.e., 1.6 mm-3 %-1–6 h and 1.6 mm-3 %-6–6 h) during the first 1.5 h of diffusion was very close. This may be explained by the fact that no overlap between the diffusion areas of adjacent pores occurred during the first 1.5 h of diffusion in the 6-pore

network.

The diffusion experiments indicated that the number of pores had the most significant impact on the diffusion behavior of the contrast agent used, followed by the pore size and hydrogel concentration. Various combinations of parameters can be used to produce the desired diffusion behavior. Based on our results regarding the effects of various parameters on the diffusion behavior of such constructs, the local concentrations and diffusion distances at different time points can be tailored to realize a controllable perfusion by this platform. In addition, designing pores with different sizes on the same branch with an optimized interspace may enable achieving differential concentrations of the same agent in different locations with high precision.

To this end, a 3D mesh diagram was generated to depict the normalized concentration of the contrast agent diffusing through pores with diameters of 1.6 mm and 0.8 mm for the 3 % hydrogel and 6-hour diffusion period (Fig. 10a and b). The diagram may serve as a design aid for predicting the relevant values (e.g., pore size and gel concentration), allowing for the estimation of the time required to attain a specific concentration at a defined diffusion distance or determining the concentration reached at a particular vertical diffusion distance within a specified time frame. Such a physics-based, rational approach provides valuable insights for guiding the future designs of similar perfusable networks, enabling the customization of diffusion characteristics to meet specific requirements.

#### 4.3. Limitations

Some experimental limitations need to be considered when interpreting the results of the current study. This study focused on fabricating multi-scale networks for *in vitro* tissue culture, utilizing three additive manufacturing methods: FDM, SLA, and 2PP. While these methods were chosen, it is worth noting that alternatives, such as powder bed fusion and volumetric printing [52] can also achieve network preparation. Additionally, the characterization of diffusion, a key function of the network, was conducted using three key parameters namely pore size, number of pores, and alginate concentration, with each experiment involving three specimens to conclude. Nevertheless, expanding the specimen number could enhance the robustness of the conclusions.

The constant-concentration boundary condition was used to study diffusion as much as possible independently from other mass transport mechanisms. In practice, *in situ* constant-concentration diffusion experiments are less challenging experimentally than *in situ* constant-flux or more complex boundary conditions. For future cell experiments, perfusion will likely be required. While the discrepancy between the model system studied here and the one likely used in cell experiments

can be considered a limitation of the current study, it is important to realize that perfusion is expected to accelerate mass transport further, thereby assisting in cell nutrition and oxygenation.

In the selection of the contrast agent, the uncharged iodixanol-based contrast agent was selected as our model compound. In future tests, it would also be interesting to choose contrast agents with different charges, such as positively or negatively charged, to study the effect of charge on diffusion. Alternatively, a wider selection of hydrogels can be applied. For example, alginate carries a negative charge [53]. By choosing hydrogels with different charges or crosslinking methods, the impact of hydrogel charge and contrast agent charge on the diffusion behavior can be studied. Nevertheless, the investigation of diffusion behavior of two distinct model systems underscores the capability of the designed porous networks to enable controlled spatiotemporal diffusion of various molecules into hydrogels with different properties. In addition, it reveals the versatility of the proposed platform that allows quantitative evaluation of diffusion by using two different methods, namely micro-CT and fluorescence microscopy, which are frequently used in the fields of tissue engineering and regenerative medicine.

#### 5. Conclusions

We used three types of additive manufacturing techniques (i.e., FDM, SLA, and 2PP) to fabricate rationally designed 3D multi-channel perfusable networks that enable sustained in vitro tissue in 3D tissue models at different length scales. For each method, the optimum printing conditions were identified based on the resulting geometric fidelity of three different network designs (i.e., single-channel networks, multi-channel networks, and dendritic networks). The findings highlighted the role of printing speed and temperature (FDM), printing angle (SLA), and hatching and slicing distances (2PP) in determining the geometric fidelity of the resulting networks. The diffusion experiments combined with contrast agent-enhanced micro-CT analyses revealed that the number of pores per channel has the most significant impact on the diffusion behavior of the studied contrast agent, followed by variations in the pore size and hydrogel concentration. Furthermore, the experimental results followed Fick's law of diffusion and enabled the prediction of diffusion distances and concentration profiles for specific pore sizes. Taken together, the findings of this study set the technological and methodological basis for the development of novel tailor-made networks that can be incorporated into 3D tissue models for sustaining in vitro tissue growth.

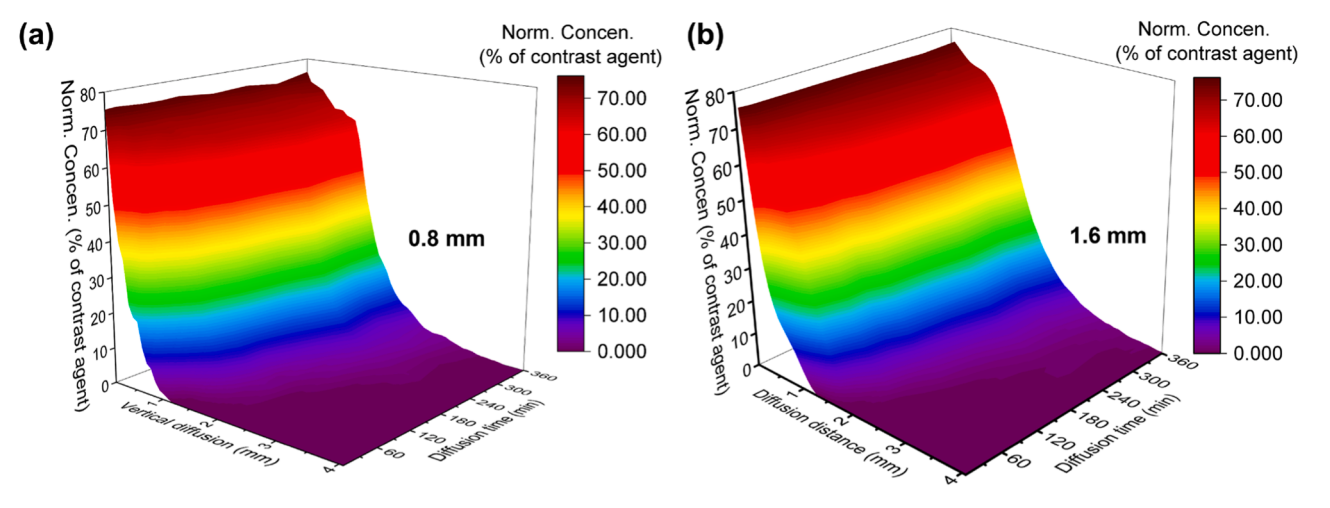


**Fig. 10.** 3D diagram of the normalized concentration as a function of vertical diffusion distance and diffusion time for pore diameters of 0.8 (a) mm and 1.6 (b) mm. All the other conditions were the same (*i.e.*, 3 % hydrogel and a 6-hour diffusion period).

#### CRediT authorship contribution statement

J. Li: Writing – review & editing, Writing – original draft, Software, Methodology, Formal analysis, Data curation, Conceptualization. A. Isaakidou: Writing – review & editing, Methodology, Investigation. L.J. van Zanten: Data curation, Formal analysis. R.P. Tas: Formal analysis, Methodology. M.J. Mirzaali: Writing – review & editing, Validation, Supervision, Software, Project administration, Methodology, Conceptualization. L.E. Fratila-Apachitei: Writing – review & editing, Validation, Supervision, Project administration, Methodology, Investigation, Conceptualization. A.A. Zadpoor: Writing – review & editing, Validation, Supervision, Software, Resources, Project administration, Methodology, Funding acquisition, Conceptualization.

#### Declaration of competing interest

The authors declare that they have no known competing financial interests or personal relationships that could have appeared to influence the work reported in this paper.

The author is an Editorial Board Member/Editor-in-Chief/Associate Editor/Guest Editor for this journal and was not involved in the editorial review or the decision to publish this article.

### Acknowledgments

J.L. thanks China Scholarship Council (CSC) for financial support.

#### Supplementary materials

Supplementary material associated with this article can be found, in the online version, at doi:10.1016/j.actbio.2025.03.005.

#### References

- D.J. Maltman, S.A. Przyborski, Developments in three-dimensional cell culture technology aimed at improving the accuracy of in vitro analyses, Biochem. Soc. Trans. 38 (4) (2010) 1072–1075.
- [2] C.M. Moysidou, C. Barberio, R.M. Owens, Advances in engineering human tissue models, Front. Bioeng. Biotechnol. 8 (2021) 620962.
- [3] M. Hofer, M.P. Lutolf, Engineering organoids, Nature Rev. Mater. 6 (5) (2021)
- [4] D.E. Ingber, Human organs-on-chips for disease modeling, drug development and personalized medicine, Nature Rev. Genetics 23 (8) (2022) 467–491.
- [5] J.M. Wilkinson, A review of complex in vitro cell culture stressing the importance of fluid flow and illustrated by organ on a chip liver models, Front. Toxicol. 5 (2023) 1170193.
- [6] M.R. Carvalho, D. Lima, R.L. Reis, J.M. Oliveira, V.M. Correlo, Anti-cancer drug validation: the contribution of tissue engineered models, Stem Cell Rev. Rep. 13 (2017) 347–363.
- [7] C.L. Chaffer, R.A. Weinberg, A perspective on cancer cell metastasis, Science 331 (6024) (2011) 1559–1564.
- [8] T.Q. Huang, X. Qu, J. Liu, S. Chen, 3D printing of biomimetic microstructures for cancer cell migration, Biomed. MicroDevices 16 (2014) 127–132.
- [9] Y. Zhao, R. Yao, L. Ouyang, H. Ding, T. Zhang, K. Zhang, S. Cheng, W. Sun, Threedimensional printing of Hela cells for cervical tumor model in vitro, Biofabrication. 6 (3) (2014) 035001.
- [10] J. Chen, X. Zhang, R. Millican, T. Lynd, M. Gangasani, S. Malhotra, J. Sherwood, P. T. Hwang, Y. Cho, B.C. Brott, G. Qin, Recent progress in in vitro models for atherosclerosis studies, Front. Cardiovasc. Med. 8 (2022) 790529.
- [11] A.J. Ribeiro, Y.S. Ang, J.D. Fu, R.N. Rivas, T.M. Mohamed, G.C. Higgs, D. Srivastava, B.L. Pruitt, Contractility of single cardiomyocytes differentiated from pluripotent stem cells depends on physiological shape and substrate stiffness, Proc. Natl. Acad. Sci. 112 (41) (2015) 12705–12710.
- [12] M.N. Hirt, A. Hansen, T. Eschenhagen, Cardiac tissue engineering: state of the art, Circ. Res. 114 (2) (2014) 354–367.
- [13] H. Tani, S. Tohyama, Human engineered heart tissue models for disease modeling and drug discovery, Front. Cell Dev. Biol. 10 (2022) 855763.
- [14] S.N. Bhatia, G.H. Underhill, K.S. Zaret, I.J. Fox, Cell and tissue engineering for liver disease, Sci. Transl. Med. 6 (245) (2014), 245sr2-245sr2.
- [15] K.H. Lee, J. Lee, S.H. Lee, 3D liver models on a microplatform: well-defined culture, engineering of liver tissue and liver-on-a-chip, Lab. Chip. 15 (19) (2015) 3822–3837.
- [16] X. Liu, X. Wang, L. Zhang, L. Sun, H. Wang, H. Zhao, Z. Zhang, W. Liu, Y. Huang, S. Ji, J. Zhang, 3D liver tissue model with branched vascular networks by multimaterial bioprinting, Adv. Healthc. Mater. 10 (23) (2021) 2101405.

[17] H. Hu, H. Gehart, B. Artegiani, C. LÖpez-Iglesias, F. Dekkers, O. Basak, J. van Es, S. M.C. de Sousa Lopes, H. Begthel, J. Korving, M. van den Born, Long-term expansion of functional mouse and human hepatocytes as 3D organoids, Cell 175 (6) (2018) 1591–1606

- [18] T. Takebe, K. Sekine, M. Enomura, H. Koike, M. Kimura, T. Ogaeri, R.R. Zhang, Y. Ueno, Y.W. Zheng, N. Koike, S. Aoyama, Vascularized and functional human liver from an iPSC-derived organ bud transplant, Nature 499 (7459) (2013) 481–484.
- [19] A.J. Miller, J.R. Spence, In vitro models to study human lung development, disease and homeostasis, Physiology 32 (3) (2017) 246–260.
- [20] Y.M. Choi, H. Lee, M. Ann, M. Song, J. Rheey, J. Jang, 3D bioprinted vascularized lung cancer organoid models with underlying disease capable of more precise drug evaluation, Biofabrication. 15 (3) (2023) 034104.
- [21] N. Koike, D. Fukumura, O. Gralla, P. Au, J.S. Schechner, R.K. Jain, Creation of long-lasting blood vessels, Nature 428 (6979) (2004) 138–139.
- [22] S. Levenberg, J. Rouwkema, M. Macdonald, E.S. Garfein, D.S. Kohane, D. C. Darland, R. Marini, C.A. Van Blitterswijk, R.C. Mulligan, P.A. D'Amore, R. Langer, Engineering vascularized skeletal muscle tissue, Nat. Biotechnol. 23 (7) (2005) 879–884.
- [23] C. Fischbach, D.J. Mooney, Polymers for pro-and anti-angiogenic therapy, Biomaterials 28 (12) (2007) 2069–2076.
- [24] L.E. Bertassoni, M. Cecconi, V. Manoharan, M. Nikkhah, J. Hjortnaes, A.L. Cristino, G. Barabaschi, D. Demarchi, M.R. Dokmeci, Y. Yang, A. Khademhosseini, Hydrogel bioprinted microchannel networks for vascularization of tissue engineering constructs, Lab. Chip. 14 (13) (2014) 2202–2211.
- [25] J.D. Baranski, R.R. Chaturvedi, K.R. Stevens, J. Eyckmans, B. Carvalho, R. D. Solorzano, M.T. Yang, J.S. Miller, S.N. Bhatia, C.S. Chen, Geometric control of vascular networks to enhance engineered tissue integration and function, Proc. Natl. Acad. Sci. 110 (19) (2013) 7586–7591.
- [26] S.V. Murphy, A. Atala, 3D bioprinting of tissues and organs, Nat. Biotechnol. 32 (8) (2014) 773–785.
- [27] S.V. Murphy, A. Atala, Y.S. Zhang, K. Yue, J. Aleman, K. Mollazadeh-Moghaddam, S.M. Bakht, J. Yang, A. Khademhosseini, 3D bioprinting for tissue and organ fabrication, Ann. Biomed. Eng. 45 (2017) 148–163.
- [28] N.F. Huang, V. Serpooshan, V.B. Morris, N. Sayed, G. Pardon, O.J. Abilez, K. H. Nakayama, B.L. Pruitt, S.M. Wu, Y.S. Yoon, J.C. Zhang, Big bottlenecks in cardiovascular tissue engineering, Commun. Biol. 1 (1) (2018) 199.
   [29] B.M. Ogle, N. Bursac, I. Domian, N.F. Huang, P. Menasché, C.E. Murry, B. Pruitt,
- [29] B.M. Ogle, N. Bursac, I. Domian, N.F. Huang, P. Menasché, C.E. Murry, B. Pruitt, M. Radisic, J.C. Wu, S.M. Wu, J. Zhang, Distilling complexity to advance cardiac tissue engineering, Sci. Transl. Med. 8 (342) (2016), 342ps13-342ps13.
- [30] G. Vunjak-Novakovic, N. Tandon, A. Godier, R. Maidhof, A. Marsano, T.P. Martens, M. Radisic, Challenges in cardiac tissue engineering, Tissue Eng. Part B 16 (2) (2010) 169–187.
- [31] R.J. McMurtrey, Roles of diffusion dynamics in stem cell signaling and threedimensional tissue development, Stem Cells Dev. 26 (18) (2017) 1293–1303.
- [32] M. Radisic, J. Malda, E. Epping, W. Geng, R. Langer, G. Vunjak-Novakovic, Oxygen gradients correlate with cell density and cell viability in engineered cardiac tissue, Biotechnol. Bioeng. 93 (2) (2006) 332–343.
- [33] S. Maharjan, J. Alva, C. Cámara, A.G. Rubio, D. Hernández, C. Delavaux, E. Correa, M.D. Romo, D. Bonilla, M.L. Santiago, W. Li, Symbiotic photosynthetic oxygenation within 3D-bioprinted vascularized tissues, Matter. 4 (1) (2021) 217–240.
- [34] Z. Zhao, X. Chen, A.M. Dowbaj, A. Sljukic, K. Bratlie, L. Lin, E.L.S. Fong, G. M. Balachander, Z. Chen, A. Soragni, M. Huch, Organoids, Nature Rev. Methods Prim. 2 (1) (2022) 94.
- [35] S.A.P. Rajan, J. Aleman, M. Wan, N.P. Zarandi, G. Nzou, S. Murphy, C.E. Bishop, H. Sadri-Ardekani, T. Shupe, A. Atala, A.R. Hall, Probing prodrug metabolism and reciprocal toxicity with an integrated and humanized multi-tissue organ-on-a-chip platform, Acta Biomater. 106 (2020) 124–135.
- [36] J. Yan, Z. Li, J. Guo, S. Liu, J. Guo, Organ-on-a-chip: a new tool for in vitro research, Biosens. Bioelectron. 216 (2022) 114626.
- [37] C.M. Leung, P. De Haan, K. Ronaldson-Bouchard, G.A. Kim, J. Ko, H.S. Rho, Z. Chen, P. Habibovic, N.L. Jeon, S. Takayama, M.L.C Shuler, A guide to the organon-a-chip, Nature Rev. Methods Prim. 2 (1) (2022) 33.
- [38] I.S. Kinstlinger, S.H. Saxton, G.A. Calderon, K.V. Ruiz, D.R. Yalacki, P.R. Deme, J. E. Rosenkrantz, J.D. Louis-Rosenberg, F. Johansson, K.D. Janson, D.W. Sazer, Generation of model tissues with dendritic vascular networks via sacrificial laser-sintered carbohydrate templates, Nature Biomed. Eng. 4 (9) (2020) 916–932.
- [39] Y. Zhang, P. Kumar, S. Lv, D. Xiong, H. Zhao, Z. Cai, X. Zhao, Recent advances in 3D bioprinting of vascularized tissues, Mater. Des. 199 (2021) 109398.
- [40] D.B. Kolesky, R.L. Truby, A.S. Gladman, T.A. Busbee, K.A. Homan, J.A. Lewis, 3D bioprinting of vascularized, heterogeneous cell-laden tissue constructs, Adv. Mater. 26 (19) (2014) 3124–3130.
- [41] D.B. Kolesky, K.A. Homan, M.A. Skylar-Scott, J.A. Lewis, Three-dimensional bioprinting of thick vascularized tissues, Proc. Natl. Acad. Sci. 113 (12) (2016) 3179–3184.
- [42] Q. Gao, Z. Liu, Z. Lin, J. Qiu, Y. Liu, A. Liu, Y. Wang, M. Xiang, B. Chen, J. Fu, Y. He, 3D bioprinting of vessel-like structures with multilevel fluidic channels, ACS. Biomater. Sci. Eng. 3 (3) (2017) 399–408.
- [43] G. Gao, J.H. Lee, J. Jang, D.H. Lee, J.S. Kong, B. Kim, Y.J. Choi, W.B. Jang, Y. J. Hong, S.M. Kwon, D.W. Cho, Tissue engineered bio-blood-vessels constructed using a tissue-specific bioink and 3D coaxial cell printing technique: a novel therapy for ischemic disease, Adv. Funct. Mater. 27 (33) (2017) 1700798.
- [44] C.A. Schneider, W.S. Rasband, K.W. Eliceiri, NIH image to ImageJ: 25 years of image analysis, Nat. Methods 9 (7) (2012) 671–675.
- [45] John. Crank, The Mathematics of Diffusion, 2nd ed., Oxford University Press, 1975.

- [46] Robert C. McOwen, \*Partial Differential Equations\*, Pearson Education, 2003.
- [47] R. Xie, V. Pal, Y. Yu, X. Lu, M. Gao, S. Liang, M. Huang, W. Peng, I.T. Ozbolat, A comprehensive review on 3D tissue models: biofabrication technologies and preclinical applications, Biomaterials (2024) 122408.
- [48] A. Kafle, E. Luis, R. Silwal, H.M. Pan, P.L. Shrestha, A.K. Bastola, 3D/4D printing of polymers: fused deposition modelling (FDM), selective laser sintering (SLS), and stereolithography (SLA), Polymers 13 (18) (2021) 3101.
- [49] S.H. Kim, C.C. Chu, Pore structure analysis of swollen dextran-methacrylate hydrogels by SEM and mercury intrusion porosimetry, J. Biomed. Mater. Res. 53 (3) (2000) 258–266.
- [50] J. Li, D.J. Mooney, Designing hydrogels for controlled drug delivery, Nature Rev. Mater. 1 (12) (2016) 1–17.
- [51] N. Kanpipit, N. Nualkaew, W. Kiatponglarp, A. Priprem, S. Thapphasaraphong, Development of a sericin hydrogel to deliver anthocyanins from purple waxy corn cob (Zea mays L.) extract and in vitro evaluation of anti-inflammatory effects, Pharmaceutics 14 (3) (2022) 577.
- [52] V. Sgarminato, J. Madrid-Wolff, A. Boniface, G. Ciardelli, C. Tonda-Turo, C. Moser, 3D in vitro modeling of the exocrine pancreatic unit using tomographic volumetric bioprinting, Biofabrication 16 (4) (2024) 045034.
- [53] J.D. Boerckel, Y.M. Kolambkar, K.M. Dupont, B.A. Uhrig, E.A. Phelps, H.Y. Stevens, A.J. García, R.E. Guldberg, Effects of protein dose and delivery system on BMPmediated bone regeneration, Biomaterials 32 (22) (2011) 5241–5251.